

# Formation Mechanism of Elemental Te Produced in Tellurite Glass Systems by Femtosecond Laser Irradiation

Gözden Torun,\* Tetsuo Kishi, Diego Pugliese, Daniel Milanese, and Yves Bellouard

The formation of elemental trigonal tellurium (t-Te) on tellurite glass surfaces exposed to femtosecond laser pulses is discussed. Specifically, the underlying elemental crystallization phenomenon is investigated by altering laser parameters in common tellurite glass compositions under various ambient conditions. Elemental crystallization of t-Te by a single femtosecond laser pulse is unveiled by high-resolution imaging and analysis. The thermal diffusion model reveals the absence of lattice melting upon a single laser pulse, highlighting the complexity of the phase transformation. The typical cross-section displays three different crystal configurations over its depth, in which the overall thickness increases with each subsequent pulse. The effect of various controlled atmospheres shows the suppressing nature of the elemental crystallization, whereas the substrate temperature shows no significant impact on the nucleation of t-Te nanocrystals. This research gives new insight into the elemental crystallization of glass upon femtosecond laser irradiation and shows the potential to fabricate functional transparent electronic micro/nanodevices.

## 1. Introduction

Tellurium (Te) is a naturally occurring elemental van der Waals material that has a p-type narrow band gap semiconductor behavior and features a chiral structure in an atomic level.<sup>[1]</sup> It has a trigonal crystal structure with three atoms in the unit cells, which are covalently bonded forming elongated helical chains, side-linked one to another by weak van der Waals forces. The typical helical chain structure spirals around the z-direction, with three-fold rotational and translational symmetry. Depending on the chains' helicity, either left- or right-handed (i.e., space groups of  $P3_121$  and  $P3_221$ , respectively), the material exhibits a chirality-dependent behavior.<sup>[2–5]</sup> Te has gained considerable interest because of its unique structure originating mainly from its electronic structure with four 5p-orbital valence electrons in the outer shell, with two 5s-lone-pair electrons<sup>[6]</sup> that lead to particularly attractive piezoelectric,<sup>[7]</sup> thermoelectric,<sup>[8]</sup> photoconductive<sup>[9]</sup> strain-sensitive,<sup>[5]</sup> and nonlinear optical responses.<sup>[10]</sup> Promising devices have been reported recently, such as low-dimensional field-effect transistors,<sup>[10–12]</sup> energy harvesters, and photothermal converters.<sup>[13,14]</sup>

To unleash the technological potential of Te, one has to master the production at the nanoscale. However, producing thin films, nanosheets, nanorods, nanowires, and nanoparticles remains challenging.<sup>[15]</sup> Numerous processes have been proposed, including chemical vapor deposition (CVD),<sup>[16]</sup> hydrothermal method,<sup>[10]</sup> molecular beam epitaxy,<sup>[17,18]</sup> solution-based growth,<sup>[19]</sup> vapor phase synthesis, growth vapor trapping,<sup>[12]</sup> with many recent efforts on pulsed laser deposition,<sup>[20]</sup> magnetron sputtering,<sup>[21]</sup> and liquid exfoliation.<sup>[22]</sup> In addition, few studies showed the production of Te starting from its amorphous oxide counterpart ( $\text{TeO}_2$ ). The formation of Te from tellurite (or  $\text{TeO}_2$ -based) glass has been observed in a handful of studies where researchers employed electrochemical charging–discharging<sup>[23,24]</sup> and femtosecond laser direct-write processing,<sup>[25–27]</sup> the approach discussed herein. In the previous work, we showed the formation of localized Te embedded in self-organized nanostructures, oriented perpendicular to the laser polarization, that span beyond the focal volume, and the evolution of nanostructures on the tellurite glass surface upon femtosecond laser exposure.<sup>[25]</sup> Here, we further investigate the in-depth formation mechanism of laser-induced elemental Te and, in particular, the effect of the substrate composition, the

the

G. Torun, Y. Bellouard

Galatea Laboratory

STI/IEM

Ecole Polytechnique Fédérale de Lausanne (EPFL)

2002 Neuchâtel, Switzerland

E-mail: gozden.torun@epfl.ch

T. Kishi

Department of Materials Science and Engineering

Tokyo Institute of Technology

Tokyo 152–8552, Japan

D. Pugliese

Department of Electronics and Telecommunications

Polytechnic University of Turin

10129 Turin, Italy

D. Pugliese

Department of Applied Science and Technology and INSTM RU

Polytechnic University of Turin


10129 Turin, Italy

D. Milanese

Department of Engineering and Architecture and INSTM RU

University of Parma

43124 Parma, Italy

 The ORCID identification number(s) for the author(s) of this article can be found under <https://doi.org/10.1002/adma.202210446>.

© 2023 The Authors. Advanced Materials published by Wiley-VCH GmbH. This is an open access article under the terms of the Creative Commons Attribution License, which permits use, distribution and reproduction in any medium, provided the original work is properly cited.

DOI: 10.1002/adma.202210446

substrate temperature, and ambient conditions for various laser processing parameters. Our findings reveal the formation of Te not only on the surface as nanoparticles but also below it as nanocrystals embedded in the tellurite glass. The most surprising fact is the observation of elemental Te nanocrystals after a single laser pulse, which is remarkable considering the extremely short time scale. In the sequel, we unravel the formation mechanism of elemental Te in common tellurite glass compositions. This work is meant to expand the realm of production of Te nanoparticles by offering a framework for selecting appropriate glass composition with relevant laser parameters and, at the same time, to document illustrations of ultrafast glass decomposition and elemental crystallization.

## 2. Results and Discussion

### 2.1. General Methodology

Experimental details are presented in a separate section at the end of this paper. Briefly, our methodology is exposing the surface of the carefully selected tellurite glass compositions to ultrafast laser pulses of varying intensity to create laser-modified tracks to highlight the formation mechanism. First, the effect of laser pulse-to-pulse overlapping, a way to effectively determine the number of pulses per focal volume in a dynamic laser writing process, is discussed to understand the feedback mechanism on the elemental crystallization and structural modifications. Second, the effect of heat generated during ultrafast laser processing on the nucleation and the growth of elemental nanocrystals from single pulse to multi-pulse per focal volume is examined. In addition, the effect of an open-air atmosphere (nitrogen, oxygen, and humidity) is investigated by comparing it with a controlled dry air atmosphere, a dry nitrogen atmosphere, and a vacuum. Likewise, the effect of substrate temperature is explained briefly. For these parts of the study, we consider the following composition: 80TeO<sub>2</sub>–10WO<sub>3</sub>–10K<sub>2</sub>O (mol%, TWK). The laser processing window (incoming pulse fluence vs repetition rate) is presented in Figure S1, Supporting Information. Finally, the effect of glass modifiers on elemental crystallization is considered in various tellurite glass systems with an effort to generalize the elemental crystallization phenomenon.

### 2.2. Formation of t-Te on Tellurite Glass Surface: From a Single Pulse to a Few Pulses Exposure

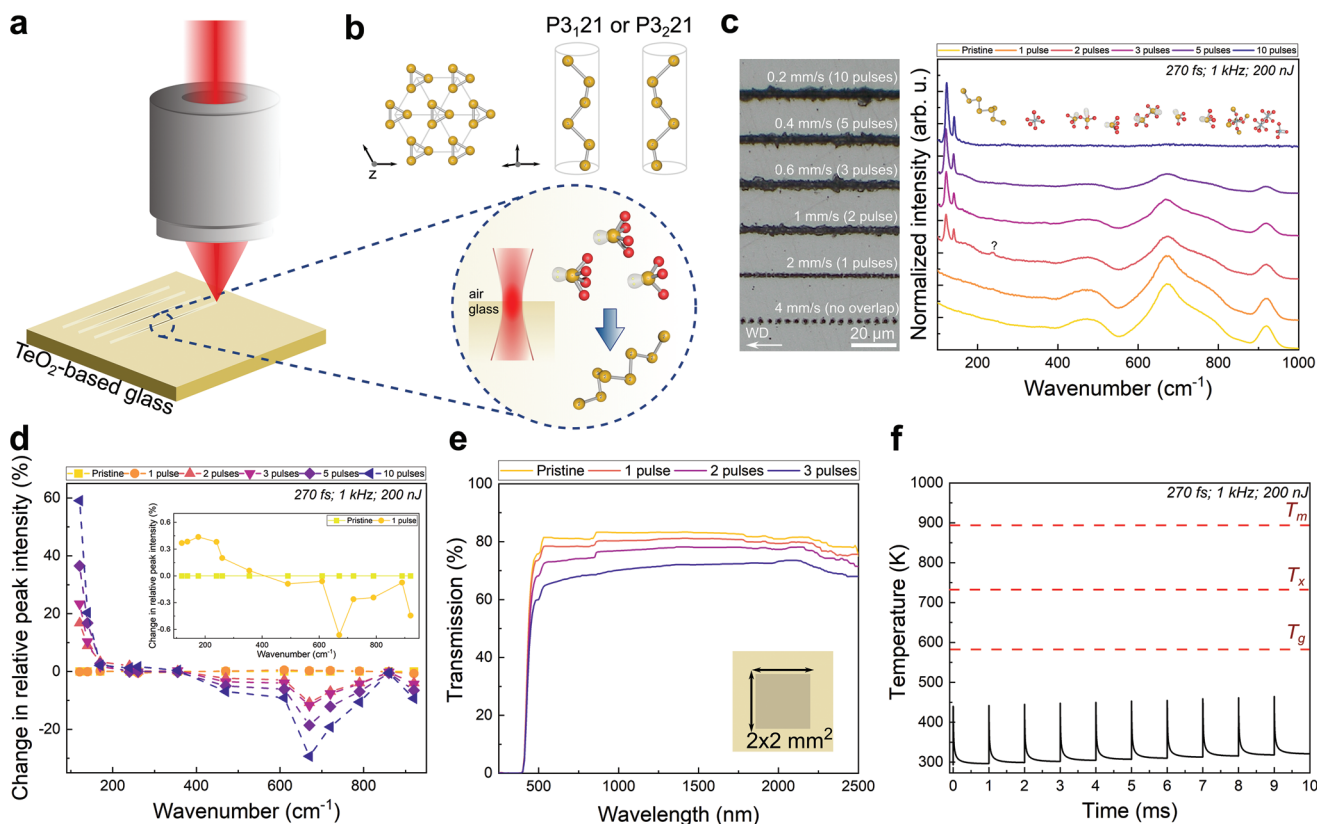
Let us first examine the case of single to a few pulses exposure, that is, from no to gradual accumulation of pulses, for which we investigate the structural evolution using Raman and UV–VIS spectroscopies. The rationale of these investigations is to unravel stepwise mechanisms leading to the formation of t-Te.

Figure 1a,b presents a schematic illustration of the typical laser processing, the atomic structure of Te, and the structural evolution of the tellurite glass surface after the inscription. Figure 1c–e shows characteristic features and spectroscopy results after single to a few laser pulse exposure of the tellurite glass surface. Figure 1c displays the optical microscopy (OM)

images and the Raman spectra of the laser-modified zones on the surface of tellurite glass. At 1 kHz, the effective number of pulses at the focal volume increases from a single pulse to ten pulses, subsequently forming continuous tracks.

As a glass, tellurite has a peculiar glass network that comes from the active free lone-electron pairs, responsible for the high refractive index and non-linear optical transmission in the IR region.<sup>[28]</sup> The free lone-electron pairs in TeO<sub>n</sub> polyhedra are the reason why forming a pure tellurium dioxide (TeO<sub>2</sub>) glass phase is difficult to obtain under traditional quenching conditions. Vitrification can be facilitated by introducing new structural units and forming mixed Te–O–R (in our case R = W, Nb, etc.) bonds. Studies have shown that the “pure” TeO<sub>2</sub> glass consists of TeO<sub>4</sub> trigonal bipyramids (tbp) and TeO<sub>3</sub> trigonal pyramids (tp) units.<sup>[29,30]</sup> The increase of glass modifier content causes the transformation of TeO<sub>4</sub> into TeO<sub>3</sub> along with the creation of non-bridging oxygen (NBO) atoms, with one of the equatorial positions occupied by the lone pair of electrons. Therefore, the glass network of TWK is composed of TeO<sub>4</sub> tbp, TeO<sub>3+1</sub> distorted trigonal bipyramids (d-tbp), and TeO<sub>3</sub> tp units. It results in the presence of Raman peaks located at around 470, 610, 670, 720, and 790 cm<sup>−1</sup>, and assigned to a symmetrical stretching of Te–O–Te linkages, continuous network of TeO<sub>4</sub>, antisymmetric stretching of Te–O–Te linkages consisting two unequivalent Te–O bonds, Te and NBO of TeO<sub>3+1</sub> and TeO<sub>3</sub>, stretching of Te–O<sup>−</sup> in TeO<sub>3+1</sub> and TeO<sub>3</sub>, respectively.<sup>[31]</sup> Depending on the glass composition, additional peaks can originate from glass modifiers. For instance, in TWK, Raman peaks at around 355, 860 and 920 cm<sup>−1</sup> are related to tungsten-oxygen vibration, that is, the stretching of W–O–W, W–O, W–O<sup>−</sup>, and W=O bonds associated with WO<sub>4</sub> and WO<sub>6</sub> polyhedra.<sup>[31,49]</sup> All these units are considered the backbone of the glass structure, whose intensity decreases with the appearance of the peaks at lower wavenumbers after femtosecond laser irradiation.

We note the presence of vibration peaks corresponding to t-Te after two effective pulses per focal volume in Figure 1c,d. The characteristic vibration peaks of the laser-affected zone are located at 118, 139, and 260 cm<sup>−1</sup>, corresponding to A<sub>1</sub> and E<sub>2</sub> modes, and second-order spectra, respectively.<sup>[30]</sup> Another broad peak at around 170 cm<sup>−1</sup> is attributed to Te–Te homopolar bonds in amorphous Te (a-Te). The a-Te observed in Raman spectra could survive even though a-Te is unstable above 285 K<sup>[31]</sup> due to higher stress around the interface, yet, it can be found up to 473 K<sup>[32]</sup> in some compounds of Te. In a different set of experiments, Vasileiadis et al.<sup>[33]</sup> reported the short-live presence of a-Te (similar peak at around 170 cm<sup>−1</sup>) during the first exposure of tellurium to continuous wave lasers (at visible wavelengths) at low power density. In addition, a peak at around 238 cm<sup>−1</sup> may originate from ionized Te dimers (Te<sub>2</sub><sup>−</sup> color center) or Te<sub>2</sub> or Te<sub>n</sub> clusters.<sup>[34–36]</sup> Another possible identification of this peak is TeO<sub>3</sub><sup>2−</sup> (specifically the –OH units in the hydrogen bonding of (TeO<sub>3</sub>)<sup>2−</sup> units<sup>[37]</sup>) at the expense of those with higher wavenumbers, indicating that the glass network is progressively cleaved. A few other studies state that this peak may also be related to the formation of WO<sub>3</sub> crystals,<sup>[38,39]</sup> rhombohedral-TeO<sub>3</sub>,<sup>[40]</sup> or β-TeO<sub>2</sub> crystals.<sup>[41]</sup> Interestingly, this peak appears at every even pulse up to ten pulses and eventually disappears from Raman spectra when the femtosecond



**Figure 1.** A schematic illustration of elemental Te production by femtosecond laser inscription on TeO<sub>2</sub>-based glass and its characterization at 1 kHz. a) Femtosecond (fs) laser direct-write process. b) The crystal structure of t-Te and the formation process of t-Te. c) OM image and Raman spectra on the surface of TWK glass upon femtosecond laser inscription at 1 kHz with 200 nJ, and from no overlap to 10 pulses (incoming pulse fluence: 0.03–0.66 J mm<sup>-2</sup>). d) The relative intensity change of main glass network peaks measured at the center of the laser-affected zone for each inscription indicated in (a). The inset image shows the change in relative peak intensity upon single laser exposure. e) The transmission spectra of the scanned area of 2 × 2 mm<sup>2</sup> with a different number of pulse per focal volume. f) Simulated temporal evolution of the temperature at 1 kHz.

laser process is performed in an open-air atmosphere. Figure 1d shows the changes in relative peak intensities extracted from Raman spectra in Figure 1c. The evolution of the peak to the effective number of pulses highlights a dramatic increase in the t-Te at the expense of the glass network. The decomposition of this peak is discussed further in detail.

The UV–Vis transmission spectra of a laser-inscribed area of 2 × 2 mm<sup>2</sup> on the tellurite glass surface in Figure 1e indicate that the UV cut-off wavelength was at around 460 nm (corresponding to 2.7 eV). The transmission spectra are progressively decreasing due to the formation of t-Te after each pulse. Compared to Raman spectra results, UV–Vis spectra results represent the gradual change in the glass structure upon a single pulse to two-pulse irradiation.

The time-dependent temperature distribution of focal volume calculated by thermal diffusion<sup>[44]</sup> of multi-pulse irradiation at 1 kHz is shown in Figure 1f. The temperature rises quickly in the focal volume, and thermal quenching with a typical cooling rate of  $\approx 10^{14}$  K s<sup>-1</sup> eventually leads to supercooling of new dense phases, and/or metastable phases recovered under extreme conditions.<sup>[45]</sup> As the pulse interval (1 ms) is longer than the lattice cooling time, the temperature rise is not affected by the second pulse. We note that the modification created upon the first pulse changes the overall material properties

within the focal volume, resulting in different thresholds, ionization rates, etc., for upcoming pulses.

A similar laser exposure at 1 kHz was performed on the glass with a temperature ranging from 77 to 293 K. The sample was cooled with liquid nitrogen in a designated chamber to avoid possible thermal effects. The Raman spectra of pristine glass and three-pulse exposure at 77 K are presented in Figure S2, Supporting Information. No particular difference in Raman spectra of the laser-affected zone at room temperature or below is observed, showing the sort of athermal nature of the elemental crystallization or “phase separation” process.

Figure 2a–c shows the transmission electron microscopy (TEM) images (including high-resolution TEM or HR-TEM) after a single laser pulse. The overall selected area electron diffraction (SAED) pattern in Figure 2a shows a bright amorphous ring with several polycrystalline diffraction spots. The crystallized width is  $\approx 1$   $\mu$ m, and the overall depth is  $\approx 350$  nm. The laser-affected zone shows three different crystal arrangements over its depth, namely, ejected and subsequently resolidified nanoparticles, densely packed nanocrystals, and scattered spherical nanocrystals, respectively. The different morphology of nanocrystals along the depth is related to the laser processing itself, similar to a recent study<sup>[44]</sup> of Cu ablation by femtosecond laser. The temperature decreases exponentially along



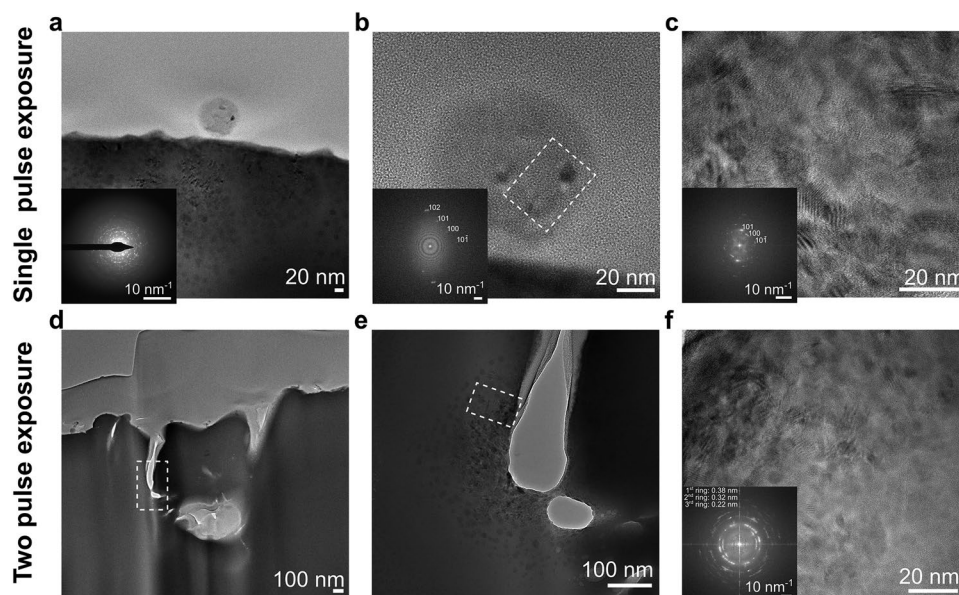


**Figure 2.** a–c) Single pulse exposure case. a) TEM image of the overall laser-affected zone within the focal volume with the inset image being the SAED pattern. b) HR-TEM image of a nanoparticle in (a) with inset images of FFT patterns oriented along the crystallographic [010] axis and c) HR-TEM image of the subsurface. Inset images are showing FFT patterns along the [010] crystallographic axis. d–f) Two-pulse exposure case: d) TEM images of overall the focal volume and e) details of the laser-affected zone; f) HR-TEM image of the subsurface zone with inset images of FFT patterns. The glass composition is TWK and the pulse energy for both cases is 200 nJ at 1 kHz.

the *z*-direction, resulting in a different cooling rate. The average size of the densely packed nanocrystals is  $5.3 \pm 1.4$  nm, located at the first 143 nm below the surface. Below these nanocrystals, the scattered spherical nanocrystals are present without overlapping each other.

Figure 2b shows an ejected particle, whose appearance is rare in single laser pulse irradiation. The Fast Fourier transform (FFT) of the image indicates the presence of a nanocrystalline phase of *t*-Te along [100] direction, even though most of the particles remain in an amorphous state, possibly due to the presence of glass structures. Figure 2c shows an HR-TEM image of the center of the laser-affected zone with densely packed nanocrystals of polycrystalline *t*-Te along [100] direction, showing characteristic double diffraction patterns (Moiré fringes) in a spatially confined area. Moiré fringes, typically with spacing an order of magnitude higher than the original ones, may originate from the superposition of repetitive nanocrystals of *t*-Te with very small or equal spacing with suitable mutual orientation. Their thickness depends on the spacing of the interacting lattices, the misfit, and the angle formed.<sup>[47]</sup> The high lattice mismatch is related to laser-induced stress. A prominent example is twisted bi-layer graphene, which forms Moiré fringes at a particular angle and exhibits superconductivity and other electronic properties.<sup>[48]</sup>

Figure 2d–f shows the TEM and HR-TEM images upon two pulses per focal spot. With the second pulse, the surface roughness increases, and the formation of a cavity becomes prominent, filled with redeposited material. Similar to a single pulse exposure, three different characteristic morphologies along its depth are observed. The average size of the densely packed nanocrystals is  $6.5 \pm 2.8$  nm. Several crystal orientations coexist in the FFT image of Figure 2f. The interplanar

distances of the nanocrystal are 0.385, 0.323, and 0.222 nm, which are in good agreement with the value of (100), (101), and (110) of the *t*-Te crystal structure. The lattice parameters from the SAED correspond to  $a = 0.4447$  nm and  $c = 0.5915$  nm. Details of interplanar distances and TEM analysis for a few laser shots are shown in Table S1 and Figure S3, Supporting Information. There is no other crystalline phase detected in the laser-affected zone rather than *t*-Te, corroborating the Te-related nature of the extra vibration peak at  $\approx 238$   $\text{cm}^{-1}$  in the Raman spectra.

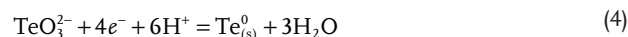
Tellurite glass is known as conditional glass former, which requires glass modifier oxides to make an amorphous network. TWK glass system is selected for this study due to its extremely large glass-forming window.<sup>[29]</sup> Depending on the glass modifier oxides, for example, the addition of K results in cleavage of Te–O–Te bonds and generates NBO sites, whereas W substitutes Te and Te–O–W bond formation enhances glass against devitrification in our case.<sup>[29,47]</sup> One of the requirements from the laser processing to obtain *t*-Te from a tellurite glass is to use laser pulse in the femtosecond regime (270 fs) with a high peak intensity emitting near-IR wavelength to satisfy the nonlinear absorption, which subsequently leads to ionization processes. The effect of the nonlinear ionization process is investigated by exposing the same glass with the femtosecond laser emitting UV wavelength (343 nm; 450 fs) and pulsed CO<sub>2</sub> laser irradiation (10.6  $\mu\text{m}$ ; 1  $\mu\text{s}$  to 1 ms). The Raman spectra in Figure S4, Supporting Information show the signature peaks of TeO<sub>2</sub> crystals, similar to the results obtained from the annealing process.<sup>[48]</sup> The results highlight the importance of the interaction time and the non-linear absorption mechanism. The proposed formation mechanism of *t*-Te from tellurite glass under a few pulses is as follows:

1) During femtosecond laser irradiation, the plasma is seeded by the multiphoton absorption process ( $\approx$ three photons) and fed through avalanche ionization of the electrons excited to the conduction band. In the present case, the plasma consists of a high concentration of Te ions upon bond cleavage. Upon the first pulse, the self-seeding reduction reaction of  $\text{Te}^{4+}$  to  $\text{Te}^0$  occurs. It has been reported that once the smallest cooperative group of molecules ( $\text{Te}_n$  clusters) consisting of two or more Te atoms together is established, it leads to the formation of crystalline structures through glass decomposition or “phase separation” of Te. Interestingly, a similar mechanism has been reported for Te-compounds and alloys, such as Te–Se or Cd–Te–Se alloys.<sup>[49,50]</sup> Upon the formation of multiple Te clusters, strong interchain bonding results in a decreased energetic requirement, and thus a higher Te content is more prone to crystallization. Since the chain-to-chain bonding strength is higher in Te due to the unlocalized electrons, this can indicate that the interchain contributions increase as the glass contains more Te content.<sup>[51]</sup> According to the configurational entropy model, Te–O–Te network bonds are weak in tellurite glass, and bond breaking can occur upon annealing around glass-transition temperature ( $T_g$ ).<sup>[29]</sup> In our case, while Te makes Te–Te bonds, oxygen ions can form molecular oxygen ( $\text{O}_2$  (g)) as observed in other glass systems,<sup>[52]</sup> and also can make a bond with the glass modifiers. The charge neutrality is satisfied by the selective oxidation of the other species, such as the conversion of  $\text{WO}_4$  units to  $\text{WO}_5$  or  $\text{WO}_6$  units. In addition, W–O bonds are much stronger than Te–O bonds, therefore, higher energy is required to break the bond. The Gibbs free energy change,  $\Delta G$ , of tungsten oxide is much lower than tellurium oxide, making  $\text{WO}_3$  formation more favorable and promoting the reduction of  $\text{TeO}_2$  into Te.<sup>[53,54]</sup>

2) As the material is modified gradually in the focal volume, the subsequent laser pulse encounters with transformed material each time. The following pulse will be less efficiently captured by the material, due to scattering by the surface roughness introduced previously.<sup>[57]</sup> Hence, the absorption efficiency will be lower for the second pulse. In addition, the absorption mechanism is altered by the presence of t-Te nanocrystals in the focal volume, whose band gap is 0.34 eV (the bandgap of the glass is  $\approx$ 3 eV). Upon the second pulse, the peak at  $\approx 238\text{ cm}^{-1}$  in Raman spectra in Figure 1 can be due to  $\text{Te}_2$  or/and  $\text{Te}_n$  clusters, or interaction between species of Te–O with relative humidity, resulting in –OH groups in  $(\text{TeO}_3)^{2-}$  unit. As mentioned in the first step, the self-reduction reaction of Te accompanied by the formation of  $\text{Te}_n$  clusters consisting of two or more Te atoms leads to the formation of crystalline structures of Te. In addition, upon the second pulse, a large cavitation is generated, promoting the interaction between a larger surface area and the open-air atmosphere. The large surface area interacts with the open-air atmosphere, which is also the crucial step for the deoxygenation of tellurite glass network units. The following chemical reactions can occur in the plasma:



The other potential assignment of the peak at  $238\text{ cm}^{-1}$  is –OH groups in  $(\text{TeO}_3)^{2-}$  units, which can be formed during the bond cleaving of the glass network, such as  $\text{TeO}_4$ ,  $\text{TeO}_{3+1}$ , and  $\text{TeO}_3$ . The origin of –OH groups can be from the dangling bonds on the surface inherently or the relative humidity in the open-air atmosphere during the fs-laser process. In our case, the glass substrates were produced in a protected atmosphere with raw materials with a high-purity. After glass production and stress relief treatment, the substrates were heated to 423 K for a few hours in the furnace to remove any chemically bonded water and –OH groups from the surface. Later, glass substrates were kept in a dry air atmosphere until the femtosecond laser exposure. In addition, it has previously been shown that tellurite glass exhibits strong resistance against relative humidity.<sup>[58]</sup> However, the interaction with the species in an open-air atmosphere in the plasma cannot be excluded completely. Therefore, the following reactions may have occurred while the plasma was present and facilitated Te formation in the open-air atmosphere:<sup>[59]</sup>



3) In theory, this reaction can go as long as there is a source of Te in the focal volume, such as  $\text{TeO}_4$ ,  $\text{TeO}_{3+1}$ , and  $\text{TeO}_3$  units. Let us now examine the stopping mechanism of the t-Te formation. Figure 3a shows the t-Te content at the focal volume and modified depth depending on the number of effective pulses. After forming t-Te, the concentration of t-Te rises exponentially up to ten pulses in the laser-affected zone and decays in the glass network, which in turn affects the formation of t-Te nanocrystals and the degree of supersaturation. After the tenth pulse, the saturation indicates the completion of the conversion of the glass network to t-Te at the focal volume. The saturation mechanism is due to nucleation-induced concentration depletion in the focal volume. When the degree of supersaturation of Te is relatively low, several seeds can accumulate together to form t-Te nanocrystals. Yet, the higher degree of supersaturation causes slower nucleation kinetics of t-Te nanocrystals. Another reason is the formation of an anisotropic surface nanostructure, which makes non-uniform electric field distribution. The final reason is that by the nanocrystal formation, the physical properties of the focal volume are altered. The proposed scenarios of tellurite glass composition and the formation of t-Te under a few pulses are schematically represented in Figure 3b.

### 2.3. Formation of t-Te on Tellurite Glass Surface: Thermal-Cumulative Exposure

Let us now consider the case when the time between pulses is shorter than the lattice cooling time constant, which typically occurs in a few  $\mu\text{s}$ .<sup>[58]</sup> The purpose of this part of the study is to observe the effect of temperature on the formation of t-Te nanocrystals and their growth. Figure 4a shows the time-dependent temperature distribution of the focal volume calculated using the thermal diffusion model<sup>[42]</sup> for the case of

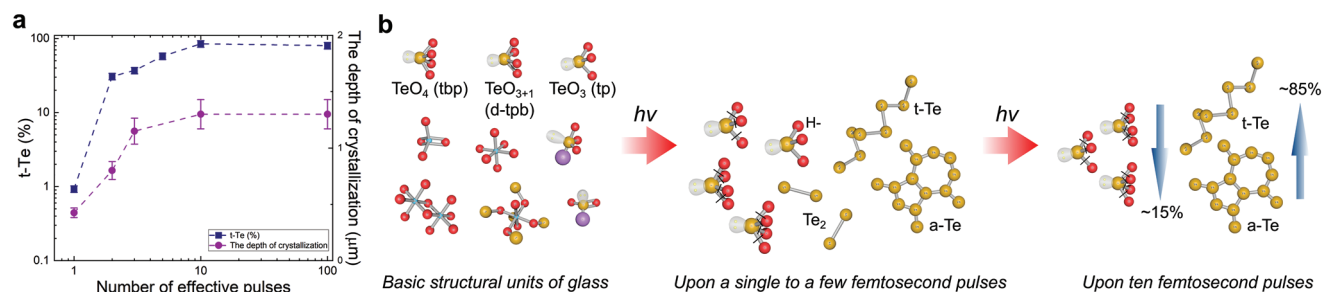


**Figure 3.** a) The percentage of t-Te Raman peaks ( $I_{118,139,260}$ ) at the laser-affected zone of TWK glass and the maximum depth of t-Te to the number of effective pulses (measured from TEM images). b) Schematic representation of the possible scenarios of polyatomic-ions migration processes and the formation of t-Te under a few pulses.

multi-pulse irradiation at 1 MHz. Tellurite glass under the 3D enclosure of a laser focal volume is subjected to high pressure and temperature. Under our experimental conditions, since the arrival of the next pulse (1  $\mu\text{s}$ ) is shorter than the lattice cooling time, the thermal accumulation regime is observed, subsequently leading to a melting of the glass surface.

Raman spectra (Figure 4b) performed across the laser-exposed side indicate the presence of multiple phases, blending crystalline and amorphous phases. The pristine glass peaks are

found around 355, 490, 610, 670, 720, 790, 860, and 920  $\text{cm}^{-1}$ ,<sup>[31,49]</sup> still present in the Raman spectra and consequently still present in the probed volume. Additional peaks of t-Te after laser exposure are located at 118, 139, and 260  $\text{cm}^{-1}$ .<sup>[32]</sup> Another peak located at 170  $\text{cm}^{-1}$  is attributed to Te–Te homopolar bonds in a-Te. Further details about the laser parameters in the thermal-cumulative regime have been presented in our previous work.<sup>[25]</sup> Detailed information on the deconvolution

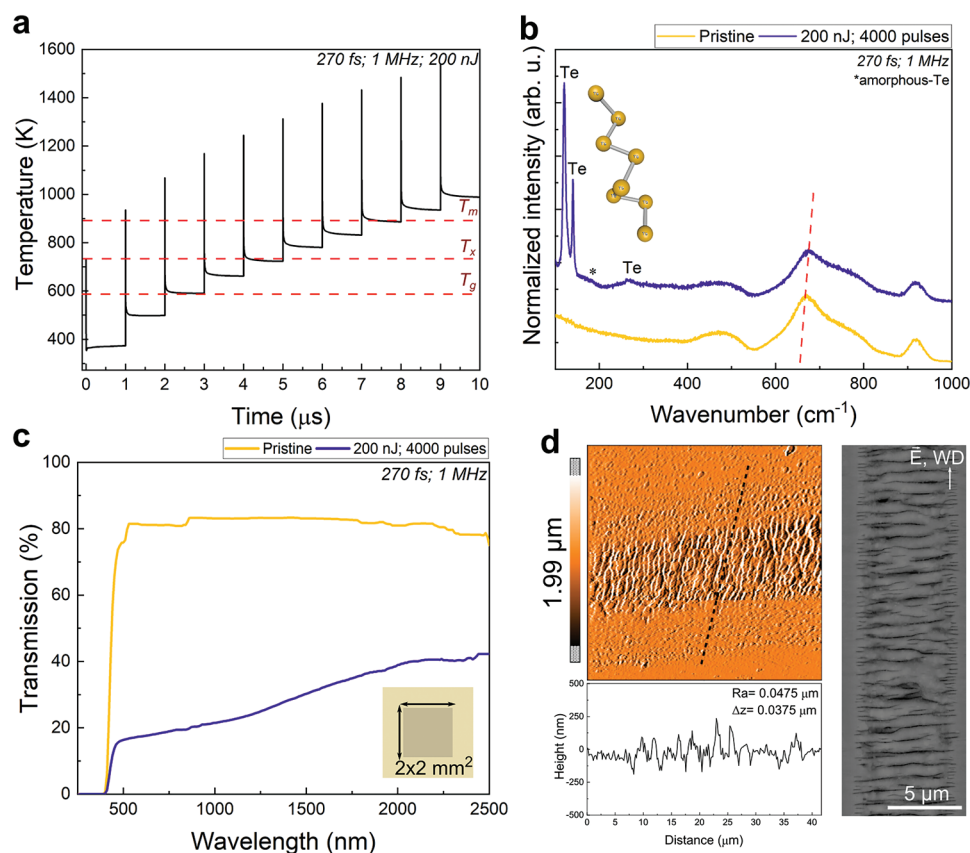


**Figure 4.** a) Temporal temperature evolution during the first ten pulses within the focal volume. The dashed lines indicate the glass transition ( $T_g$ ), crystallization ( $T_x$ ), and melting ( $T_m$ ) temperature of TWK glass. b) Raman spectra of pristine TWK glass and the center of the laser-affected zone indicated in (a). c) UV–Vis transmission spectra of TWK glass (thickness of 2 mm) and after the laser exposure of 200 nJ with  $\approx 4000$  pulses (incoming pulse fluence: 262  $\text{J mm}^{-2}$ ). Inset: The schematic of laser-scanned area (2  $\times$  2 mm<sup>2</sup>) on TWK glass for UV–Vis spectroscopy. d) Atomic force microscopy (AFM) image of surface nanostructures at 40.6  $\times$  40.6  $\mu\text{m}^2$  area with z-direction intensity of 1.99  $\mu\text{m}$  and back-scattered electron (BSE) image of the surface of TWK glass.



of Raman spectra is presented in Figure S5, Supporting Information.

The transmission spectra of the pristine glass and the laser-affected zone are presented in Figure 4c. The reason for the vast reduction in the transmission is the formation of t-Te, photodarkening due to rearrangement in the glass structure, increase in reflection and scattering due to surface nanostructures and nanoparticles. Figure S6, Supporting Information shows the corresponding absorption spectra of the pristine glass and the laser-affected zone. As for the Te nanoparticles,<sup>[14]</sup> the absorption spectrum of the laser-affected zone shows broadband absorption with two distinct peaks around 400 and 1000 nm. The self-organized nanostructures perpendicular to the laser polarization, and ejected nanoparticles, which are byproducts of laser exposure, are shown in Figure 4d.

Figure 5 shows back-scattered electron (BSE) and TEM images of the laser-affected zone on the tellurite glass surface upon multi-pulse femtosecond laser inscription at the thermal accumulation regime. The typical BSE image of self-organized surface structures perpendicular to the laser polarization is presented in Figure 5a. Figure 5b illustrates the TEM image of the cross-section of the laser-affected zone with the schematic of the laser focal point. Figure 5c shows the TEM image of the tellurite glass surface at the border of the focal volume with an inset image of the SAED pattern. The SAED pattern presents the polycrystalline nature of the area, which contains ejected nanoparticles with subsurface nanocrystals. The relatively large grains result in bright single diffraction spots, whereas the ring

pattern originates from several nanocrystals with different crystallographic orientations. The details of the SAED pattern can be found in Table S2 and Figure S7, Supporting Information. The X-ray diffraction (XRD) pattern of the SAED pattern shows a slight shift from t-Te (Te-I), which corresponds to t-Te (Te-I) at 2 GPa.<sup>[59]</sup> Undefined weak diffractions point out a possible match with the Te-II phase,<sup>[60]</sup> although further confirmation is needed with advanced characterization techniques. The electron-lattice energy transfer in the fs-laser process results in lattice heating in  $\mu\text{s}$  time scale with shock wave (pressure-wave) generation. The pressure is estimated to be around a few TPa in the volume of the fused silica and on its surface when it is irradiated by fs-laser with an energy density of  $40 \text{ J cm}^{-2}$ .<sup>[61]</sup> The generated pressure results in high-density silica<sup>[62]</sup> and a new crystalline phase<sup>[63]</sup> in fused silica or elemental aluminum formation<sup>[64]</sup> in the sapphire ( $\alpha\text{-Al}_2\text{O}_3$ ). Additionally, the surface cracks along the laser writing direction upon fs-laser irradiation in Figure S8 indicate the stress level exceeds Young's modulus of tellurite glass ( $\approx 42 \text{ GPa}$ ).<sup>[65]</sup>

From surface to subsurface, there are three different characteristics along its depth similar to the ones at 1 kHz, that are, nanoparticles, densely packed irregularly shaped nanocrystals, and spherical nanocrystals. Figure 5d presents the morphology of typical ejected particles with an inset of the FFT pattern. Crystalline nanoparticles indicate the material ejection after the surface melting, re-solidification, and re-deposition to the surface. The HR-TEM and SAED confirm that nanoparticles display excellent crystallinity of [100] t-Te with an average diameter of 54 nm. Figure 5e–g shows TEM images of the center of the

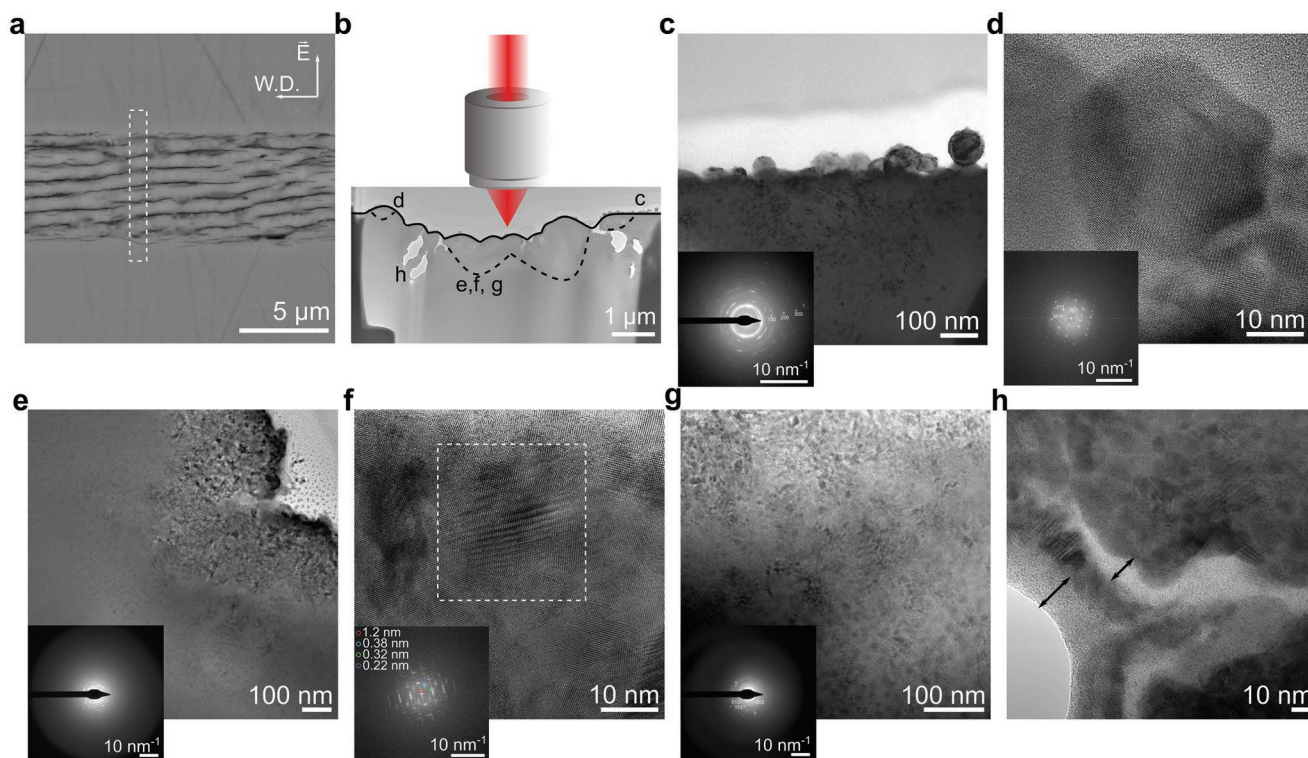


**Figure 5.** a) BSE image of self-organized nanostructures on the surface of TWK glass upon laser inscription at 1 MHz with 200 ns and 4000 pulses (incoming pulse fluence:  $262 \text{ J mm}^{-2}$ ). b) TEM image of the cross-section indicated by a dashed line in (a) with the schematic of the laser focal point. c) TEM image of the surface with an inset image of the SAED pattern. d,e) HR-TEM image of the ejected particles and subsurface with inset images of FFT patterns. The zone axis of (d) is [100]. f,g) TEM images of the laser-affected zone at focal volume with inset images of SAED patterns with the zone axis of [031] and h) TEM image of nanostructures in the volume. The location of (c)–(h) images is marked in (b).

laser-affected zone at focal volume with inset images of SAED patterns. The SAED pattern in Figure 5e reveals a polycrystalline t-Te phase. (Unidentified diffractions spots found together with the diffraction spots of t-Te are presented in Figure S7, Supporting information). Similarly, those diffractions fit well with Te-I with a weak signal of Te-II rather than the oxide polymorphs of Te and any known compounds of each element present in the pristine material.<sup>[32,61,62,68–70]</sup> The results are not surprising since at least tens of GPa of pressure is generated on the surface of dielectrics upon the femtosecond laser process, yet, it needs advanced techniques to confirm high-pressure Te phases. It is assumed that the peak pressure at the front of the shock wave driven by the laser is at least a few times the pressure value necessary to induce structural phase changes near the point where the energy is deposited. The first subsurface layer in Figure 5f shows densely packed irregularly distributed nanocrystals with double diffraction. The interplanar spacings of the nanocrystals are 1.2, 0.38, 0.32, and 0.22 nm, corresponding to the double diffraction of (001), the diffraction of (100), (101), and (110) of the t-Te structure, respectively. The average nanocrystal size is  $12.78 \pm 2.84$  nm. Below the first  $\approx 330$  nm, the scattered spherical nanocrystals are located without overlapping each other. The interface between two types of nanocrystalline morphology is shown in Figure 5g. The interplanar spacings are 0.38 and 1.75 nm, corresponding to (100) and (013), respectively. The average thickness of the third layer is 420 nm. The SAED pattern of the scattered spherical nanocrystals exhibits also diffraction of t-Te.

Another characteristic of laser modification on the surface of dielectrics is the formation of self-organized nanocracks, perpendicular to the laser polarization.<sup>[71]</sup> The cracks were enlarged during TEM lamella preparation by focused ion beam (FIB), and hence, their dimensions after the milling appear larger than they actually are. The nanocracks under the surface are surrounded by alternating amorphous and polycrystalline t-Te layers, as displayed in Figure 5h. The very first layer of 10–20 nm is an amorphous material. Polycrystalline layers show Moiré fringes due to the same reason mentioned above. The polycrystalline t-Te around nanocracks has densely packed irregularly distributed spherical morphology similar to the ones observed in the first layer of the laser-affected zone. We note that the oxidation of the t-Te nanocrystals into TeO<sub>2</sub> crystals in a multi-pulse regime is not detected by Raman spectroscopy and is not observed in high-resolution imaging.

The above investigation showed the formation of nanocrystals in extreme conditions, such as high temperature and pressure upon 4000 pulses at 1 MHz. The crystallinity of the ejected nanoparticles is improved. The number and the average size of particles increase with the multi-pulse exposure; the average size of nanocrystals is slightly larger than the one at a few kHz. The effect of the thermal-cumulative regime on the grain growth and connectivity of the nanocrystals can be tested, for example, by nano-tomography, high-resolution XRD techniques (synchrotron radiation), or electrical resistivity measurement. The DC resistivity is tested on a single laser-inscribed track with a length of 10 mm, and the results obtained by 4-probe measurement are presented in Table 1. The electrical resistivity of the laser-affected zone at the thermal-cumulative regime exhibits the lowest value, similar to polycrystalline bulk Te.<sup>[72,73]</sup>

**Table 1.** The electrical resistivity of the laser-irradiated tracks on the surface of TWK glass with various laser-writing conditions. Note that the length of the laser tracks is 10 mm, and the cross-sectional area was calculated from TEM analysis.

Laser processing parameters	DC resistivity ( $\Omega$ m)
1 kHz; 200 nJ; 10 pulses (incoming pulse fluence: $0.66 \text{ J mm}^{-2}$ )	188.143
1 kHz; 200 nJ; 4000 pulses (incoming pulse fluence: $262 \text{ J mm}^{-2}$ )	0.53981
100 kHz; 200 nJ; 4000 pulses (incoming pulse fluence: $262 \text{ J mm}^{-2}$ )	0.16028
1 MHz; 200 nJ; 4000 pulses (incoming pulse fluence: $262 \text{ J mm}^{-2}$ )	0.00445

#### 2.4. Conditions Suppressing the Formation of t-Te (Presented in the Cumulative Regime)

So far, upon femtosecond laser writing process under an open-air atmosphere, the formation of the laser-induced defects may indicate the interaction of the glass surface with an ambient environment. The purpose of this part of the study is to investigate the effect of environmental conditions on the formation of Te, a crucial step for establishing a general understanding. For this part of the study, the laser inscription was performed on a TWK glass sample in a sealed chamber with a controlled dry air atmosphere [consisting of O<sub>2</sub>(g) and N<sub>2</sub>(g)], a dry pure nitrogen atmosphere [N<sub>2</sub>(g)], and a vacuum ( $<10^{-3}$  Pa). The results are compared with the open-air atmosphere [consisting of O<sub>2</sub>(g), N<sub>2</sub>(g), and relative humidity level of 40%, which is constantly measured].

Figure 6 shows the experimental setup, the Raman spectra of the laser-affected zone, the relative intensity ratio of the main peaks, and possible scenarios of polyatomic-ions migration processes occurring at the tellurite glass surface upon femtosecond laser inscription under various atmospheres. Figure 6a presents the experimental setup of the sealed chamber used in this study for different atmospheres. The same laser exposure conditions were applied with the same laser for all four atmospheric conditions. At 1 kHz with two-pulse irradiation, the sharp peak at  $238 \text{ cm}^{-1}$  exists in the Raman spectra (not shown here) for all atmospheric conditions. Figure 6b shows the Raman spectra of the laser-affected zone under open-air, dry air, dry nitrogen, and under a vacuum at 1 MHz. Compared to irradiation in open-air, the peak at  $\approx 238 \text{ cm}^{-1}$  is present in dry air, a vacuum, and dry nitrogen conditions, whose intensity varies as follows:  $I_{\text{nitrogen}} > I_{\text{vacuum}} > I_{\text{dry air}}$ . The surface of the glass substrates was free from chemically bonded water and –OH groups before the laser irradiation. Therefore, the experimental results under various atmospheres indicate that the origin of the peak at  $\approx 238 \text{ cm}^{-1}$  can be only Te dimers or Te<sub>n</sub> clusters. Even though the nature of the peak is identified, the intensity of the t-Te peaks at 119, 139, and  $260 \text{ cm}^{-1}$  decreases with an increase in the intensity of  $238 \text{ cm}^{-1}$  peak in Figure 6c. This evidence indicates that the presence of open-air atmosphere (including relative humidity) plays a significant role in the formation of Te and supports the reduction reactions (3) and (4).

Let us examine the laser irradiation under dry nitrogen flow, which shows the minimum level of t-Te formation. Figure 6d,e shows the Raman spectra of the laser-affected zone irradiated under dry nitrogen and the intensity ratios of the Raman peaks



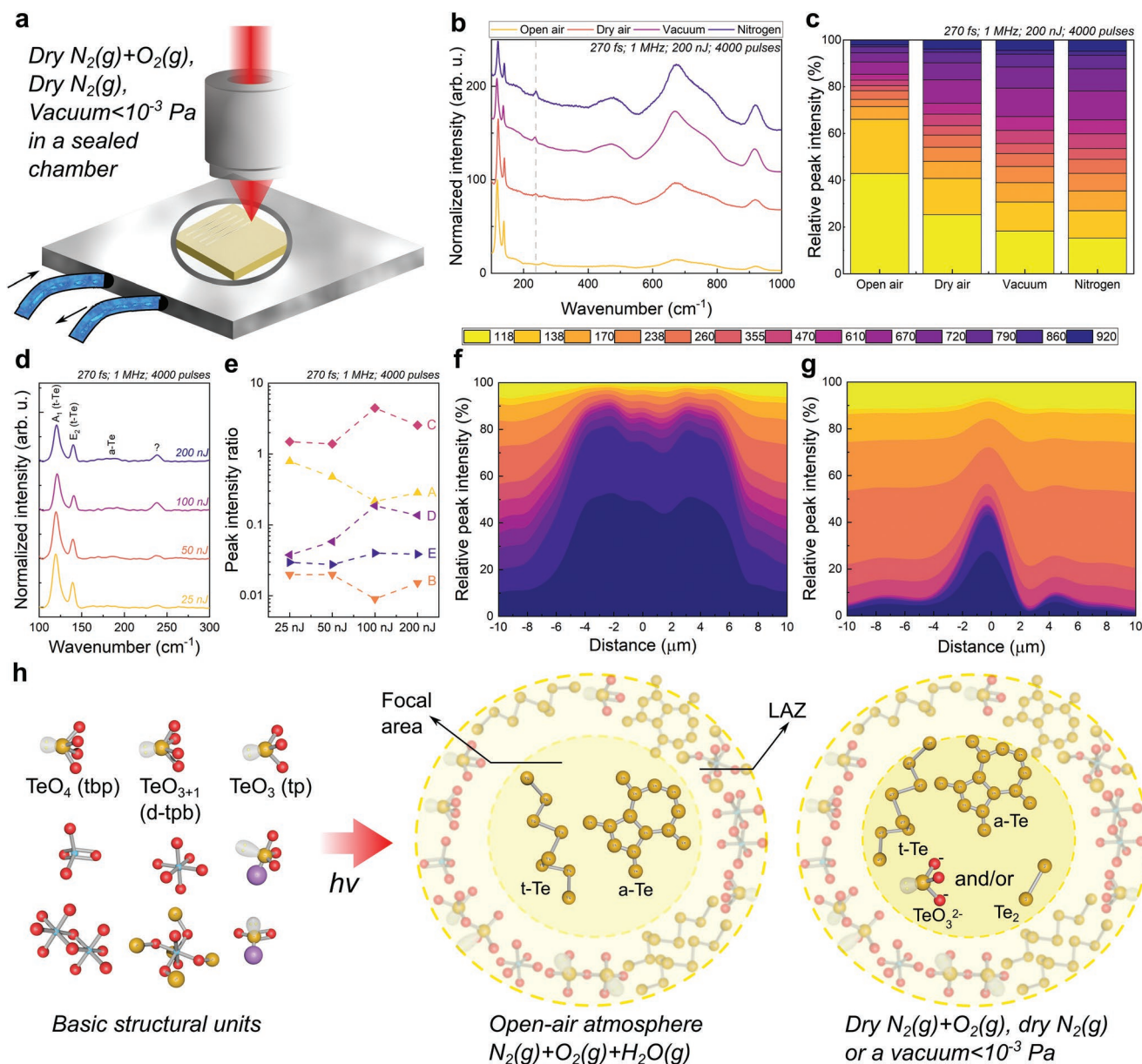


**Figure 6.** a) A schematic representation of experimental setup with a sealed chamber. b) Normalized Raman spectra of the center of the laser-affected zone under different atmospheres at 1 MHz. c) The relative intensity of the main peaks along the laser-affected zone under different atmospheres. d) Normalized Raman spectra of the center of the laser-affected zone under the dry nitrogen atmosphere. The laser parameters are 4000 pulses at various energies (25, 50, 100, and 200 nJ; incoming pulse fluence from 33 to 262  $\text{J mm}^{-2}$ ) at a rate of 1 MHz on the surface of TWK glass. e) The intensity ratio of the peaks. "A"–"E" indicate the peak intensity ratios of t-Te/glass, a-Te/glass, 238  $\text{cm}^{-1}$ /a-Te, 238  $\text{cm}^{-1}$ /t-Te, and 238  $\text{cm}^{-1}$ /glass, respectively. f, g) Spatial distribution of the ratio of peaks along the laser-affected zone, prepared under open-air atmosphere (f) and a constant dry nitrogen flow (g) at 25 nJ with 4000 pulses (incoming pulse fluence: 33  $\text{J mm}^{-2}$ ). h) Schematic representation of the t-Te formation under different atmospheres.

(A to E are the fractions of t-Te/glass, a-Te/glass, 238  $\text{cm}^{-1}$ /a-Te, 238  $\text{cm}^{-1}$ /t-Te, and 238  $\text{cm}^{-1}$ /glass, respectively). Under open-air exposure, the peak at 238  $\text{cm}^{-1}$  disappears upon exposure to ten pulses at 1 kHz. Even at lower pulse energy, the focal volume is converted into t-Te. However, after exposure to 4000 pulses under dry nitrogen flow, the peak is still present, whose intensity increases with the pulse energy. The presence of 238  $\text{cm}^{-1}$  indicates that the conversion of tellurite glass units to t-Te in the laser-affected zone is not completed effectively. Note that the polarizability of the molecules can decrease

under different atmospheres, resulting in lower peak intensity in Raman spectra. To validate the suppression of t-Te formation under dry nitrogen flow, interpreted from Raman data, a 4-probe electrical measurement is performed to the laser-affected zone inscribed under nitrogen. Under the same conditions as in Table 1 (200 nJ with 4000 pulses at 1 MHz; incoming pulse fluence of 262  $\text{J mm}^{-2}$ ), the DC resistivity of the laser-written track is 115.9  $\Omega \text{ m}$ .

Interestingly, the effect of the atmosphere has been investigated for conventional tellurite glass melting.<sup>[74]</sup> There, among

argon, oxygen, and room atmospheres,  $\text{Te}^{4+}$  ion formation is inhibited in the inert atmosphere, and more  $\text{Te}^{4+}$  concentration is obtained when the glass is prepared in an oxygen-rich atmosphere. From our experiments, we show the femtosecond laser exposure under various atmospheres resembles a similar situation as in a glass melting. Similarly, during the fiber drawing process, tellurium-doped silica fibers drawn under an argon atmosphere show a formation of  $\text{Te}_2^0$  dimers compared to fibers drawn in oxidizing conditions.<sup>[38]</sup> Although, in this case, the oxidation of  $\text{Te}_2^0$  dimer causes a diminish of this peak under an oxidizing atmosphere, in our case, oxygen is removed quickly from the laser-affected zone, leaving a plasma rich in terms of Te atoms under the laser irradiation.

A possible explanation can be that as in an open-air atmosphere, the formation of Te dimers and  $\text{Te}_n$  clusters is an essential step for the completing t-Te transformation. It means the energy delivered by each subsequent pulse is enough to break the Te–O bonds to form free Te atoms and deoxygenate the laser-affected zone. Subsequently, the abundance of Te atoms in the plasma facilitates the formation of Te nanoclusters and nanocrystals. On the contrary, under the dry nitrogen atmosphere, the transformation of Te dimers and  $\text{Te}_n$  clusters to Te nanocrystals remains challenging. It shows that oxygen and humidity (–H or –OH groups) are necessary for the reduction reaction, whose absence eventually hinders the formation of the t-Te. Note that Raman analysis did not reveal the formation of any compound containing nitrogen. Finally, Figure 6h illustrates the glass network and the final structure of the laser-affected zone under different atmospheric conditions. Post-exposure experiment shows that the irradiation atmosphere is one of the key elements to modulate the content of t-Te at the laser-affected zone.

## 2.5. Effect of the Substrate Composition

In this part of the study, we evaluate the validity of t-Te formation for all tellurite glass systems. For this purpose, common tellurite glass systems, namely  $\text{TeO}_2\text{--WO}_3\text{--Ag}_2\text{O}$  (TWA),  $\text{TeO}_2\text{--ZnO--Na}_2\text{O--BaO}$  (TZNB),  $\text{TeO}_2\text{--Nb}_2\text{O}_5\text{--GeO}_2\text{--PbO--ZnF}_2$  (TNGPZ) and  $\text{TeO}_2\text{--WO}_3\text{--K}_2\text{O}$  (TWK) are selected for their technical importance. For instance, the presence of heavy metal ions further increases the nonlinear refractive index, making the tellurite glass systems promising candidates for photonic applications, such as optical limiting and all-optical switching.<sup>[28,31]</sup> The addition of silver ions confers a high ionic conductivity, making them suitable for solid-state energy conversion applications and the immobilization of radioactive wastes in nuclear applications.<sup>[75]</sup> These glass systems are promising active materials for optical switching devices,<sup>[76]</sup> optical transistors and amplifiers,<sup>[77]</sup> acousto-optical and electro-optical components,<sup>[78]</sup> and as anodes for lithium-ion batteries (LiBs).<sup>[79]</sup> The details on the physical properties of the substrates and fs-laser modification thresholds are presented in Table S3, Supporting Information.

The Raman spectra of the laser-affected zone, the spatial distribution of relative peak intensity of t-Te, secondary electron (SE) images of the laser-affected zone, and the DC resistivity of the laser-inscribed lines in the open-air atmosphere are pre-

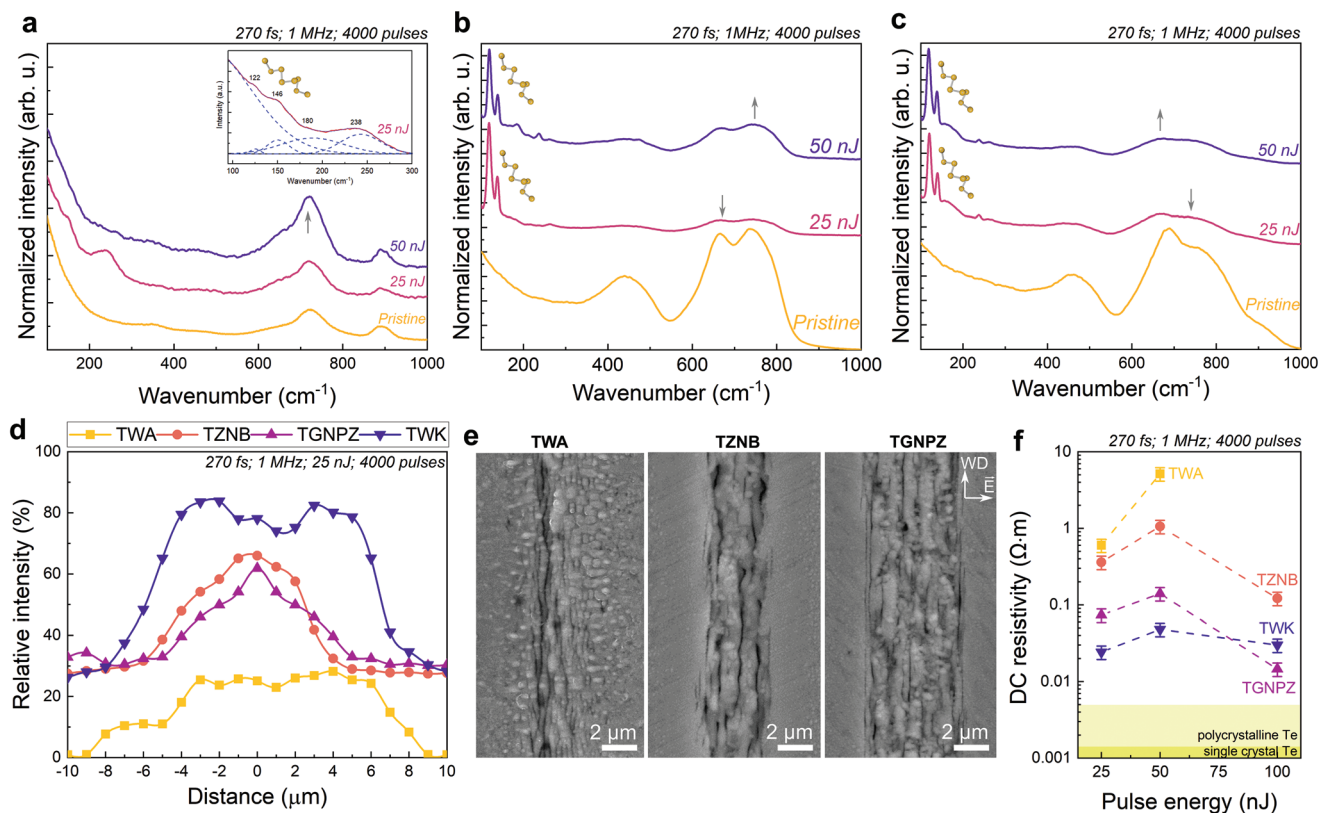
sented in Figure 7. The Raman bands and nomenclatures are summarized in Table S4, Supporting Information. Figure 7a shows the Raman spectra of the laser-affected zone in the TWA glass. A few peculiar behaviors are observed in the laser-affected zone at a pulse energy of 25 nJ. The one is the strong intensity of the boson peak, associated with the existence of nanocrystals, transversal phonons, or changes of the medium-range order (MRO).<sup>[80–82]</sup> Its position depends on the thermal or pressure history of the glass.<sup>[83]</sup> Another one is weak low wavenumber peaks, which are associated with t-Te. The peak at around  $240\text{ cm}^{-1}$  is associated with the Te dimers or  $\text{Te}_n$  clusters. At the onset of ablation (the pulse energy of 50 nJ), no peaks at low wavenumber are observed, and the main glass band gets narrower. Combined with the result of energy dispersive spectroscopy (SEM-EDS) in Figure S9, Supporting Information, the oxidation of the laser-affected zone of TWA is observed.

Figure 7b,c shows the Raman spectra of the laser-affected zone in the TZNB and TNGPZ glass systems, respectively. The increase of the peak at  $238\text{ cm}^{-1}$  is proportional with pulse energy, stimulating the reduction of the intensity ratio of t-Te/glass. Note that the peak at  $238\text{ cm}^{-1}$  in TNGPZ glass overlaps slightly with the peak at  $230\text{ cm}^{-1}$ , which is related to Nb–O–Nb bond in  $\text{NbO}_6$ . The formation of t-Te accompanied by the peak at  $238\text{ cm}^{-1}$  is a common feature in three different compositions regardless of the processing parameters in the open-air atmosphere; however, the crystal-to-glass ratio in focal volume differs.

Figure 7d shows the spatial distribution of the ratio of t-Te/glass along the laser-affected zone. The compositions of Te in TWA, TWK, TNGPZ, and TZNB glass are around 35, 60, 65, and 70 wt%, respectively. The relative intensity of t-Te at the laser-affected zone is the highest in TWK since the Te dimers and clusters are effectively converted to t-Te. The content of t-Te at the laser-affected zone in TZNB and TNGPZ is around the same as in the pristine glass, showing the almost effective transformation of  $\text{TeO}_2$ -glass to t-Te in the focal volume. Lastly, TWA exhibits the lowest elemental crystallization ratio of t-Te/glass and an extremely narrow laser-processing window.

The tellurite glass systems used in this study have a composition of Te between 35 to 70 wt% ( $\text{TeO}_2$  content is above 55 wt%). Similarly, the prerequisite for the formation of homopolar bonds of Te–Te and Te–clusters is that the Te content should be above 40 wt% for amorphous telluride alloys.<sup>[53]</sup> In addition, the amount of glass modifiers and their stability define the nature of the reaction of each element (reduction or oxidation) in the laser-affected zone. For instance, thermodynamically, in the presence of Te,  $\text{Ag}_2\text{O}$  can be reduced to Ag by Te, and lead to the  $\text{TeO}_2$  formation. These results highlight other requirements to obtain t-Te locally from tellurite glass upon femtosecond laser irradiation: the rich glass composition in terms of Te, and the quantity and the type of glass modifier oxides, which can reduce  $\text{TeO}_2$ .

Figure 7e shows the SE images of the laser-affected zone of TWA, TZNB, and TNGPZ at 1 MHz. The typical self-organized nanostructures on tellurite glass are perpendicular to the electric field of the laser, extending beyond the focal volume. Figure 7f shows the DC electrical resistivity of the laser-written tracks in the thermal-cumulative regime of all compositions. The resistivity results are close in each composition at 25 nJ.



**Figure 7.** a–c) Raman spectra of the pristine glass and the laser-affected zone of TWA (a), TZNB (b), and TGNPZ (c) at 4000 pulses with various pulse energies of 25 and 50 nJ (incoming pulse fluence of 33 and 66 J mm<sup>-2</sup>, respectively) at 1 MHz. The inset image shows the deconvolution of the lower wavenumbers of TWA. d) Spatial distribution of the ratio of t-Te/glass along the laser-affected zone at 25 nJ. e) Secondary-electron (SE) images of laser-affected zone written with 50 nJ and 4000 pulses at 1 MHz. f) The DC resistivity of the laser-written tracks of all compositions used in this study.

TZNB, TGNPZ, and TWK show a similar trend over pulse energy, whereas TWA shows a steep increase due to oxidation at the onset of ablation. Since the onset of ablation of TWK is higher than TZNB and TGNPZ, it reaches a similar value as polycrystalline bulk Te resistivity at 200 nJ (0.00445 Ω m as indicated in Table 1). These results indicate not only the potential for combining multiple material phases in a single substrate as a means for functionalizing tellurite glass but also enable the direct-write of functional 2.5D nanocomposites with physical properties easily tailored by the laser parameters. Combining its high quality and unique intrinsic properties, the t-Te/TeO<sub>2</sub> nanocomposite shows interesting properties such as photoconductivity<sup>[84,85]</sup> and ultrahigh chemical sensitivity,<sup>[86]</sup> and it is attractive for versatile applications beyond electronics and photonics.

### 3. Summary and Outlook

We have reported the formation of t-Te through femtosecond laser exposure to a tellurite glass surface for various glass compositions and both thermally cumulative and non-cumulative regimes.

Our findings on the formation of Te nanoparticles on the surface as well as Te nanocrystals under the surface upon the laser irradiation triggered the following observations:

- 1) Under our experimental exposure conditions (near-IR femtosecond laser irradiation), a single pulse is sufficient to form elemental t-Te, as revealed by high-resolution imaging and analysis.
- 2) Under the thermal-cumulative exposure regime, increasing the temperature at the focal spot promotes connectivity and grain growth in the focal volume, resulting in lower electrical resistivity.
- 3) The typical cross-section of the laser-affected zone displays three different characteristics over its depth regardless of laser parameters.
- 4) Interestingly, the formation of t-Te is greatly suppressed under a dry nitrogen atmosphere as there is limited interaction of glass network units, and the Te<sub>2</sub> or Te<sub>n</sub> clusters with an open-air atmosphere.
- 5) The formation of elemental t-Te is a common feature in all compositions; the composition should be rich in Te to obtain a large laser-processing window.

These observations highlight the complexity of the underlying phenomena sustaining the formation of a t-Te phase.

In conclusion, femtosecond laser direct-write processes offer an opportunity for producing integrated t-Te/TeO<sub>2</sub>-glass nanocomposites, particularly attractive as future functional devices fabricated without adding or subtracting any other materials, and through a single-step process. The femtosecond laser direct-write technology is simple and scalable. Here, it led to



millimeter-sized bilayer nanosheets with controllable nanostructures, physical properties, and multiple functionalities. Finally, the production of Te is favorable in an open-air atmosphere, adaptable to large-area printing of arbitrary semiconductor patterns, and suitable for photonic or electronic device fabrication.

#### 4. Experimental Section

**Glass Specimen Preparation:** Four different compositions of tellurite glass were investigated, each chosen for the relevance in various applications. All specimens were synthesized by a conventional melt-quenching technique using high-purity chemicals (99+%). After weighing and mixing, the batched chemicals were transferred into a platinum crucible and melted at 1103 K for 2 h within a muffle furnace to produce TNGPZ ( $\text{TeO}_2\text{-Nb}_2\text{O}_5\text{-GeO}_2\text{-PbO-ZnF}_2$ ) and TZNB ( $\text{TeO}_2\text{-ZnO-Na}_2\text{O-BaO}$ ) glass systems. The melts were cast into a preheated cylindrical brass mold, annealed at a temperature around the glass transition temperature for 5 h to relieve the residual internal stresses, and cooled down slowly to room temperature.  $\text{TeO}_2\text{-WO}_3\text{-Ag}_2\text{O}$  (TWA) and  $\text{TeO}_2\text{-WO}_3\text{-K}_2\text{O}$  (TWK) glass systems were produced by mixing commercial powders with high-purity and melting them in the Au crucible at around 973 K for 30 min in an electric furnace. The melts were quenched onto a brass plate. After quenching, the glass specimens were crushed and remelted at 973 K for 30 min, followed by subsequent annealing at 598 K for 1 h.

The effect of surface chemistry, and the thermal history of the substrate, which determines the level of instability/stability of the glass against crystallization are important points for glass processing.<sup>[50,87]</sup> For this work, all the glasses were stress relief treated at a temperature chosen carefully according to the composition, thus, the thermomechanical effects on the crystallization due to cooling were minimized. In addition, after stress relief treatment, all glass rods were cut and optically polished into 1–2 mm-thick specimens. Finally, the substrates were heated to 423 K for a few hours in the furnace to remove any chemically bonded water and –OH groups from the surface and kept in a dry-air atmosphere until the femtosecond laser exposure.

**Femtosecond Laser Machining:** An Yb-doped femtosecond fiber laser (Yuzu from Amplitude Laser) emitting 270 fs pulses at 1030 nm was used in this experiment. Laser patterns were inscribed on the surface of the different tellurite glasses as a line with a length of 10 mm. The specimen was translated under the laser focus with the help of a high-precision motorized stage (Ultra-HR from PI Micos). The laser beam was focused on the surface of the specimen with a 0.4 numerical aperture (NA) objective (OFR-20x-1064 nm from Thorlabs), resulting in a spot size (defined at  $1/e^2$ ) of 1.94  $\mu\text{m}$ . A wide range of pulse repetition rates (1 kHz to 1 MHz) was employed. The transition from a non-cumulative to thermal-cumulative regime was found at around 200–400 kHz. Pulse energy and translation velocity were selected as the main variables to obtain different deposited energies. Effective number of pulses is calculated as:

$$M = w \frac{f}{v} \quad (5)$$

where  $w$  is the optical beam waist (defined at  $1/e^2$ ),  $f$  is the laser repetition rate, and  $v$  is the writing speed. Accordingly, the deposited energy per unit surface (or “net fluence”) on the specimen can be approximated by:

$$E_{\text{deposited}} = \frac{4E_p}{\pi w} \left( \frac{f}{v} \right) \quad (6)$$

where  $E_p$  is the pulse energy. Here, pulse-to-pulse overlapping ratios were varying from 0 to 99.9%. The pulse energy was ranging from 1 to 500 nJ, as measured after focusing with the objective lens.

Furthermore, tracks were inscribed using opposite directions of laser beam movement along a single writing axis and under three different linear polarization states (and therefore, the orientation of the electric field  $E$ ) defined as parallel, at 45°, and perpendicular to the writing direction, respectively.

Finally, to understand the effect of the atmosphere, the laser inscription was also performed in the sealed chamber with various atmospheres. The inlet and outlet of the chamber were kept as shown in Figure 6 for constant dry air flow [ $\text{O}_2(\text{g}) + \text{N}_2(\text{g})$ , relative humidity level < 2% (industrial grade, to eliminate the condensation)] and dry nitrogen flow [ $\text{N}_2(\text{g})$ , purity > 99.9%], whereas, only inlet was kept under a vacuum ( $<10^{-3}$  Pa) in the dry chamber connected to pump. The results are compared with the open-air atmosphere [ $\text{O}_2(\text{g}) + \text{N}_2(\text{g})$ , relative humidity level is 40%, measured constantly]. To eliminate the possible moisture on the surface of the chamber (called “crystal water”), the chamber was heated to 400 K for 2 h in a furnace. In addition, desiccant salts were added in the chamber. Then, the dry chamber was flushed with constant dry nitrogen flow for 24 h before the experiment. In addition, the same chamber was used to cool down the substrate from 293 K to 77 K with liquid nitrogen to study the effect of substrate temperature on the crystallization. The same laser parameters were employed as mentioned above.

**Specimen Characterization:** After laser exposure, specimens were observed using a digital optical microscope (KH-8700 from Hirox), and subsequently, the surface profile and roughness were obtained by atomic force microscopy (AFM from Nanosurf). A Raman spectrometer (LabRam HR from Horiba), equipped with a 532 nm laser excitation source attenuated down to 4 mW was used to record Raman spectra of TWK, TZNB, and TGNPZ. For TWA glass, a Raman spectrometer (from Renishaw), equipped with a 732 nm laser excitation source attenuated down to 4 mW was used. The linearly-polarized Raman laser beam was focused at the surface of the specimen using a 0.9 NA objective (100×-532 nm and 100×-732 nm from Thorlabs). A series of line scans were performed from 10  $\mu\text{m}$  outside the laser-affected zone towards the center of the modification with a period of 1  $\mu\text{m}$ , and with acquisition times of 30 s for an individual spot. The transmission and absorption spectra were measured for wavelengths ranging from 250 to 2500 nm using an ultraviolet–visible–near-infrared spectrometer ((UV–VIS–NIR, Lambda 950 from Perkin Elmer). A mask with a hole of around  $2 \times 2 \text{ mm}^2$  was prepared from black paper for broadband absorbance. For the measurement, the reference beam power was attenuated to 10%, to compensate for the presence of the mask and the ensuing effective drastic reduction of the beam size from the original 2 cm in diameter. The thickness of the sample used for this transmission measurement was 2 mm.

For high-resolution imaging and elemental analysis, a thin film of carbon was sputtered (from JEOL) on specimens using a field-emission scanning electron microscope equipped with energy-dispersive X-ray spectroscopy (EDS) (FE-SEM, Gemini 2 from Zeiss, operated at 5 kV for imaging and 20 kV for elemental analysis). Finally, transmission electron microscope (TEM, Talos F200S from ThermoFisher) images were obtained operating at 200 kV. TEM lamellae (thickness of about 100 nm) were prepared by a focus ion beam (FIB, NVision 40 dual-beam from Zeiss), at 5 and 30 kV. FFT and SAED patterns were fitted with electron diffraction simulation of GenOVA.<sup>[88]</sup>

Finally, DC electrical resistivity was measured by a 4-probe analyzer connected to a source measurement unit (SMU B2902A from Keysight) applying a forward bias of 40 V.

**Heat Transfer Model:** The time-dependent temperature distribution model was calculated in a commercial finite element analysis software (COMSOL Multiphysics) based on a classical thermal diffusion model.<sup>[43]</sup>

$$\frac{\partial T(t, x, y, z)}{\partial t} = \nabla(D \nabla T(t, x, y, z)) + \left( \frac{1}{\rho c_p} \right) \frac{\partial Q(t, x, y, z)}{\partial t} \quad (7)$$

where  $T$  is the temperature,  $t$  is the time after laser exposure,  $D$  is the thermal diffusion coefficient,  $\rho$  is the mass density,  $c_p$  is the specific heat capacity,  $Q$  is the generated heat density calculated from the absorbed laser power density.

The initial conditions were in open-air under normal atmospheric pressure with the ambient temperature set at 293.15 K. The more accurate calculation of temperature distribution, such as via the two-temperature model (TTM) was time-consuming, and complicated since most of the parameters are unknown for the custom-made glass specimens. The energy losses came mainly from heat conduction, convection, and thermal radiation, calculated by setting the boundary conditions in COMSOL Multiphysics. The thermal properties of materials and the values used in the simulation are shown in Table S5, Supporting Information.

## Supporting Information

Supporting Information is available from the Wiley Online Library or from the author.

## Acknowledgements

The Galatea Lab is thankful to the sponsorship of Richemont International, and to Tokyo Institute of Technology and Polytechnic University of Turin for producing and providing the tellurite glass substrates. The authors are thankful to Amplitude Systèmes for providing the experimental femtosecond laser source used in this study. The authors would like to thank Dr. Pieter Vlugter for the discussion on heat transfer modeling.

Open access funding provided by Ecole Polytechnique Federale de Lausanne.

## Conflict of Interest

The authors declare no conflict of interest.

## Author Contributions

G.T. wrote the draft paper and performed most of the experiments presented in this paper, T.K. did the production of bulk materials, the first laser exposure lines, and preliminary observation for potassium-tungsten-tellurite glass, G.T. and Y.B. interpreted the experimental results, and analyzed the experimental data. T.K., D.P., and D.M. produced the pristine glass and measured various physical properties. Y.B. designed and supervised the research. All the authors discussed and revised the paper.

## Data Availability Statement

The data that support the findings of this study are available from the corresponding author upon reasonable request.

## Keywords

elemental crystallization, femtosecond laser machining, glass decomposition, tellurite glass, tellurium

Received: November 10, 2022

Revised: December 23, 2022

Published online:

- [1] G. Qiu, A. Charnas, C. Niu, Y. Wang, W. Wu, P. D. Ye, *npj 2D Mater. Appl.* **2022**, 6, 17.
- [2] Z. Y. Chen, R. Qin, *Phys. Rev. A* **2020**, 101, 53423.
- [3] A. Ben-Moshe, A. da Silva, A. Muller, A. Abu-Odeh, P. Harrison, J. Waelder, F. Niroui, C. Ophus, A. M. Minor, M. Asta, W. Theis, P. Ercius, A. P. Alivisatos, *Science* **2021**, 372, 729.
- [4] F. Calavalle, M. Suárez-Rodríguez, B. Martín-García, A. Johansson, D. C. Vaz, H. Yang, I. V. Maznichenko, S. Ostanin, A. Mateo-Alonso, A. Chuvilin, I. Mertig, M. Gobbi, F. Casanova, L. E. Hueso, *Nat. Mater.* **2022**, 21, 526.
- [5] Y. Wang, S. K. Yao, P. Liao, S. Jin, Q. Wang, M. J. Kim, G. J. Cheng, W. Wu, *Adv. Mater.* **2020**, 32, 2002342.
- [6] B. Y. Xia, P. Yang, Y. Sun, Y. Wu, B. Mayers, B. Gates, Y. Yin, F. Kim, H. Yan, *Adv. Mater.* **2003**, 15, 353.
- [7] T. Il Lee, S. Lee, E. Lee, S. Sohn, Y. Lee, S. Lee, G. Moon, D. Kim, Y. S. Kim, J. M. Myoung, Z. L. Wang, *Adv. Mater.* **2013**, 25, 2920.
- [8] S. Lin, W. Li, Z. Chen, J. Shen, B. Ge, Y. Pei, *Nat. Commun.* **2016**, 7, 10287.
- [9] P. Li, *J. Appl. Phys.* **2020**, 128, 063105.
- [10] Y. Wang, G. Qiu, R. Wang, S. Huang, Q. Wang, Y. Liu, Y. Du, W. A. Goddard, M. J. Kim, X. Xu, P. D. Ye, W. Wu, *Nat. Electron.* **2018**, 1, 228.
- [11] A. Kramer, M. L. Van de Put, C. L. Hinkle, W. G. Vandenberghe, *npj 2D Mater. Appl.* **2020**, 4, 10.
- [12] J. K. Qin, P. Y. Liao, M. Si, S. Gao, G. Qiu, J. Jian, Q. Wang, S. Q. Zhang, S. Huang, A. Charnas, Y. Wang, M. J. Kim, W. Wu, X. Xu, H. Y. Wang, L. Yang, Y. Khin Yap, P. D. Ye, *Nat. Electron.* **2020**, 3, 141.
- [13] J. Shen, S. Jia, N. Shi, Q. Ge, T. Gotoh, S. Lv, Q. Liu, R. Dronskowski, S. R. Elliott, Z. Song, M. Zhu, *Science* **2021**, 374, 1390.
- [14] C. Ma, J. Yan, Y. Huang, C. Wang, G. Yang, *Sci. Adv.* **2018**, 4, eaas9894.
- [15] Z. Shi, R. Cao, K. Khan, A. K. Tareen, X. Liu, W. Liang, Y. Zhang, C. Ma, Z. Guo, X. Luo, H. Zhang, *Nano-Micro Lett.* **2020**, 12, 99.
- [16] Q. Wang, M. Safdar, K. Xu, M. Mirza, Z. Wang, J. He, *ACS Nano* **2014**, 8, 7497.
- [17] J. Chen, Y. Dai, Y. Ma, X. Dai, W. Ho, M. Xie, *Nanoscale* **2017**, 9, 15945.
- [18] X. Huang, J. Guan, Z. Lin, B. Liu, S. Xing, W. Wang, J. Guo, *Nano Lett.* **2017**, 17, 4619.
- [19] B. Mayers, Y. Xia, *J. Mater. Chem.* **2002**, 12, 1875.
- [20] A. Apte, E. Bianco, A. Krishnamoorthy, S. Yazdi, R. Rao, N. Glavin, H. Kumazoe, V. Varshney, A. Roy, F. Shimojo, E. Ringe, R. K. Kalia, A. Nakano, C. S. Tiwary, P. Vashishta, V. Kochat, P. M. Ajayan, *2D Mater.* **2019**, 6, 015013.
- [21] E. Bianco, R. Rao, M. Snure, T. Back, N. R. Glavin, M. E. McConney, P. M. Ajayan, E. Ringe, *Nanoscale* **2020**, 12, 12613.
- [22] Z. J. Xie, C. Y. Xing, W. Huang, T. Fan, Z. Li, J. Zhao, Y. Xiang, Z. Guo, J. Li, Z. Yang, B. Dong, J. Qu, D. Fan, H. Zhang, *Adv. Funct. Mater.* **2018**, 28, 1705833.
- [23] J. Fan, Y. Zhang, G. Li, Y. Yue, *J. Non. Cryst. Solids* **2019**, 521, 119491.
- [24] Z. Jiang, T. Zhao, J. Ren, Y. Zhang, Y. Yue, *Nano Energy* **2021**, 80, 105589.
- [25] G. Torun, T. Kishi, Y. Bellouard, *Phys. Rev. Mater.* **2021**, 5, 055201.
- [26] R. G. Capelo, J. M. P. Almeida, D. F. Franco, G. Y. Poirier, C. R. Mendonça, M. Nalin, D. Manzani, *J. Mater. Res. Technol.* **2021**, 13, 1296.
- [27] C. Cheng, Y. Yu, F. Zhang, H. Zhang, J. Qiu, *J. Non-Cryst. Solids* **2014**, 406, 1.
- [28] R. A. H. El-Mallawany, *Tellurite Glasses Handbook*, CRC Press, Boca Raton, FL **2001**.
- [29] A. G. Kalampounias, G. Tsilomelekis, S. Boghosian, *J. Chem. Phys.* **2015**, 142, 154503.

- [30] M. A. T. Marple, M. Jesuit, I. Hung, Z. Gan, S. Feller, S. Sen, *J. Non Cryst. Solids* **2019**, *513*, 183.
- [31] T. Kosuge, Y. Benino, V. Dimitrov, R. Sato, T. Komatsu, *J. Non Cryst. Solids* **1998**, *242*, 154.
- [32] C. Marini, D. Chermisi, M. Lavagnini, D. Di Castro, C. Petrillo, L. Degiorgi, S. Scandolo, P. Postorino, *Phys. Rev. B* **2012**, *86*, 064103.
- [33] Y. H. Cheng, S. W. Teitelbaum, F. Y. Gao, K. A. Nelson, *Phys. Rev. B* **2018**, *98*, 134112.
- [34] R. T. Ananth Kumar, H. A. Mousa, P. Chithra Lekha, S. T. Mahmoud, N. Qamhieh, *J. Phys. Conf. Ser.* **2017**, *869*, 012018.
- [35] T. Vasileiadis, S. N. Yannopoulos, *J. Appl. Phys.* **2014**, *116*, 103510.
- [36] D. Reinen, G. G. Lindner, *Chem. Soc. Rev.* **1999**, *28*, 75.
- [37] C. Heinemann, W. Koch, *Mol. Phys.* **1997**, *92*, 463.
- [38] A. S. Zlenko, V. M. Mashinsky, V. O. Sokolov, V. V. Koltashev, N. M. Karatun, L. D. Iskhakova, S. L. Semjonov, V. G. Plotnichenko, *J. Opt. Soc. Am. B* **2016**, *33*, 675.
- [39] R. L. Frost, E. C. Keeffe, *Spectrochim. Acta, Part A* **2009**, *73*, 146.
- [40] M. R. Zaki, D. Hamani, M. Dutreuil-Colas, J. R. Duclère, O. Masson, P. Thomas, *J. Non Cryst. Solids* **2018**, *484*, 139.
- [41] M. F. Daniel, B. Desbat, J. C. Lassegues, B. Gerand, M. Figlarz, *J. Solid State Chem.* **1987**, *67*, 235.
- [42] J. Cornette, T. Merle-Méjean, A. Mirgorodsky, M. Colas, M. Smirnov, O. Masson, P. Thomas, *J. Raman Spectrosc.* **2011**, *42*, 758.
- [43] A. Zavabeti, P. Aukarasereenont, H. Tuohey, N. Syed, A. Jannat, A. Elbourne, K. A. Messalea, B. Y. Zhang, B. J. Murdoch, J. G. Partridge, M. Wurdack, D. L. Creedon, J. van Embden, K. Kalantar-Zadeh, S. P. Russo, C. F. McConville, T. Daeneke, *Nat. Electron.* **2021**, *4*, 277.
- [44] M. Shimizu, M. Sakakura, M. Ohnishi, Y. Shimotsuna, T. Nakaya, K. Miura, K. Hirao, *J. Appl. Phys.* **2010**, *108*, 073533.
- [45] E. G. Gamaly, S. Juodkazis, K. Nishimura, H. Misawa, B. Luther-Davies, L. Hallo, P. Nicolai, V. T. Tikhonchuk, *Phys. Rev., B* **2006**, *73*, 214101.
- [46] J. Xie, J. Yan, D. Zhu, G. He, *Adv. Funct. Mater.* **2022**, *32*, 2108802.
- [47] C. Cayron, *Scr. Mater.* **2021**, *194*, 113629.
- [48] M. Yankowitz, S. Chen, H. Polshyn, Y. Zhang, K. Watanabe, T. Taniguchi, D. Graf, A. F. Young, C. R. Dean, *Science* **2019**, *363*, 1059.
- [49] M. Çelikbilek Ersundu, A. E. Ersundu, M. I. Sayyed, G. Lakshminarayana, S. Aydin, *J. Alloys Compd.* **2017**, *714*, 278.
- [50] M. Çelikbilek, A. E. Ersundu, N. Solak, S. Aydin, *J. Non Cryst. Solids* **2011**, *357*, 88.
- [51] K. Itoh, *J. Solid State Chem.* **2017**, *246*, 372.
- [52] Y. M. Azhniuk, V. V. Lopushansky, Y. I. Hutyk, M. V. Prymak, A. V. Gomonnai, D. R. T. Zahn, *Phys. Status Solidi Basic Res.* **2011**, *248*, 674.
- [53] B. Sari, H. Batiz, C. Zhao, M. C. Scott, *Appl. Phys. Lett.* **2022**, *121*, 012101.
- [54] M. Lancry, B. Pommellec, J. Canning, K. Cook, J. C. Poulain, F. Brisset, *Laser Photonics Rev.* **2013**, *7*, 953.
- [55] R. J. Ackermann, E. G. Rauh, *J. Phys. Chem.* **1963**, *67*, 2596.
- [56] M. Aspiala, D. Sukhominov, P. Taskinen, *Thermochim. Acta* **2013**, *573*, 95.
- [57] A. Krywonos, J. E. Harvey, N. Choi, *J. Opt. Soc. Am. A* **2011**, *28*, 1121.
- [58] R. J. Jeng, T. Kishi, N. Matsushita, T. Yano, *Int. J. Appl. Glass Sci.* **2019**, *10*, 248.
- [59] A. E. Pasi, H. Glänneskog, M. R. S. J. Foreman, C. Ekberg, *Nucl. Technol.* **2021**, *207*, 217.
- [60] R. Gattass, E. Mazur, *Nat. Photonics* **2008**, *2*, 219.
- [61] X. Li, X. Huang, X. Wang, M. Liu, G. Wu, Y. Huang, X. He, F. Li, Q. Zhou, B. Liu, T. Cui, *Phys. Chem. Chem. Phys.* **2018**, *20*, 6116.
- [62] C. Hejny, M. I. McMahon, *Phys. Rev., B* **2004**, *70*, 184109.
- [63] H. Hu, X. Wang, H. Zhai, *J. Phys. D Appl. Phys.* **2011**, *44*, 135202.
- [64] G. Cheng, Y. Wang, J. D. White, Q. Liu, W. Zhao, G. Chen, *J. Appl. Phys.* **2003**, *94*, 1304.
- [65] S. Juodkazis, H. Misawa, E. G. Gamaly, B. Luther-Davies, A. V. Rode, L. Hallo, P. Nicolai, V. T. Tikhonchuk, *AIP Conf. Proc.* **2007**, *955*, 1041.
- [66] A. Vailionis, E. G. Gamaly, V. Mizeikis, W. Yang, A. V. Rode, S. Juodkazis, *Nat. Commun.* **2011**, *2*, 445.
- [67] M. A. Sidkey, M. S. Gaafar, *Phys. Rev., B* **2004**, *348*, 46.
- [68] C. Hejny, S. Falconi, L. F. Lundegaard, M. I. McMahon, *Phys. Rev., B* **2006**, *74*, 174119.
- [69] C. Hejny, M. I. McMahon, *Phys. Rev. Lett.* **2003**, *91*, 21.
- [70] F. Mauri, O. Zakharov, S. De Gironcoli, S. G. Louie, M. L. Cohen, *Phys. Rev. Lett.* **1996**, *77*, 1151.
- [71] J. Bonse, S. Gräf, *Laser Photonics Rev.* **2020**, *14*, 2000215.
- [72] A. Nussbaum, *Phys. Rev.* **1954**, *94*, 337.
- [73] R. W. McKay, W. E. Gravelle, *Can. J. Phys.* **1961**, *39*, 534.
- [74] A. do C. Capiotto, A. K. Rufino Souza, F. B. Costa, J. C. Silos Moraes, L. A. de Oliveira Nunes, J. R. Silva, L. H. da Cunha Andrade, S. M. Lima, *Ceram. Int.* **2021**, *47*, 32195.
- [75] C. W. Lee, J. Y. Pyo, H. S. Park, J. H. Yang, J. Heo, *J. Nucl. Mater.* **2017**, *492*, 239.
- [76] R. F. Souza, M. A. R. C. Alencar, J. M. Hickmann, R. Kobayashi, L. R. P. Kassab, *Appl. Phys. Lett.* **2006**, *89*, 171917.
- [77] S. Shen, A. Jha, X. Liu, M. Naftaly, K. Bindra, H. J. Bookey, A. K. Kar, *J. Am. Ceram. Soc.* **2002**, *85*, 1391.
- [78] Y. Li, W. Fan, H. Sun, X. Cheng, P. Li, X. Zhao, *J. Appl. Phys.* **2010**, *107*, 093506.
- [79] Y. Rao, F. Kong, Y. Zheng, Y. Deng, M. K. Tabi, X. Liang, R. Bai, X. Bi, Z. Chen, D. Wang, X. Yu, H. Jiang, C. Li, *Renewable Sustainable Energy Rev.* **2022**, *165*, 112613.
- [80] H. Shintani, H. Tanaka, *Nat. Mater.* **2008**, *7*, 870.
- [81] V. K. Malinovsky, A. P. Sokolov, *Solid State Commun.* **1986**, *57*, 757.
- [82] M. P. Belançon, G. Simon, *J. Non Cryst. Solids* **2018**, *481*, 295.
- [83] J. Schroeder, W. Wu, J. L. Apkarian, M. Lee, L. G. Hwa, C. T. Moynihan, *J. Non Cryst. Solids* **2004**, *349*, 88.
- [84] K. Oishi, K. Okamoto, J. Sunada, *Thin Solid Films* **1987**, *148*, 29.
- [85] M. Palomba, U. Coscia, G. Carotenuto, S. De Nicola, G. Ambrosone, *Phys. Status Solidi Curr. Top. Solid State Phys.* **2015**, *12*, 1317.
- [86] D. Tsiulyanu, S. Marian, V. Miron, H. D. Liess, *Sens. Actuators, B* **2001**, *73*, 35.
- [87] L. Bressel, D. de Ligny, C. Sonnevile, V. Martinez, V. Mizeikis, R. Buividas, S. Juodkazis, *Opt. Mater. Express* **2011**, *1*, 605.
- [88] C. Cayron, *J. Appl. Crystallogr.* **2007**, *40*, 1179.